scientific reports

Check for updates

OPEN

Photocatalytic properties of $BiFeO_3$ powders synthesized by the mixture of CTAB and Glycine

N. Asefi, M. Hasheminiasari✉ & S. M. Masoudpanah

Highly pure $BiFeO_3$ (BFO) powders were prepared by the solution combustion synthesis method using cetyltrimethylammonium bromide (CTAB) and glycine as fuels at various fuel-to-oxidant (φ) ratios. Microstructural characteristics, morphology, optical properties, and thermal analysis were studied by X-ray diffraction (XRD), scanning electron microscopy (SEM), diffuse reflectance spectroscopy (DRS), and differential thermal/thermogravimetry (DTA/TGA), respectively. The combusted powders prepared at different fuel content contained a small amount of impurity phases such as $Bi_{24}Fe_2O_{39}$ and $Bi_2Fe_4O_9$. During the calcination of BFO powders at 600 °C for 1 h, a nearly pure BFO phase was produced. Combusted powders photodegraded about 80% of methylene blue dye at φ = 2 through 90 min of visible light irradiation.

Single-phase $BiFeO_3$ (BFO) is a multiferroic material with distorted rhombohedral and perovskite structures exhibiting the R3c space group. Due to its ferroelectric performance at high Curie temperatures up to 830 °C and antiferromagnetic behavior under its Neel temperature of 370 °C, this material is considered for non-volatile memory devices, photovoltaics, sensors, and spintronics[1–4]. It is also known that these abundant and interesting compounds with the perovskite structure exhibit improved compositional and structural tunability[5,6]. Because of its narrow bandgap in the range of 2.2–2.8 eV and high chemical stability, BFO has been considered a visible light photocatalyst to degrade organic pollutants[7]. Many photocatalysts, such as TiO_2, ZnO, CdS, ZnS, etc., have been used to photodegrade dyes under ultraviolet (UV) light irradiation[8–13]. However, UV only spans a small portion (~4%) of the sunlight spectrum; thus, many efforts have been made to develop visible-light catalysts covering a broader range[14–19].

Impurity phases such as Bi_2O_3, $Bi_2Fe_4O_9$, and $Bi_{24}Fe_2O_{39}$ appear during the synthesis of BFO due to their phase formation kinetics. Therefore, many researchers developed various synthesis routes to remove these secondary phases. Hydrothermal methods[20,21], polymer assisted hydrothermal[22], sol–gel[23], co-precipitation[24–26], aerosol-spraying, electrospinning[27], solvothermal route[28], and solution combustion[29] were used to synthesize pure BFO.

Developing simple, environmentally safe, and energy-efficient methods to synthesize a pure BFO powder is of great interest. Solution combustion synthesis (SCS) is a simple, relatively cheap, and fast chemical process to produce various nanomaterials[30]. A self-propagating exothermic reaction occurs between the mixture of metal nitrates and different organic fuels (e.g., glycine, citric acid, urea, etc.), releasing an enormous amount of gaseous products[29].

Among different organic fuels, glycine is an amino acid that facilitates the formation of a metal ion complex in the solution owing to its carboxylic acid and amino groups at opposite ends of the molecule[31]. Likewise, Cetyltrimethylammonium bromide (CTAB) is a cationic surfactant with a high decomposition temperature that is extensively used to control particle shapes, size, and microstructure by minimizing the precursor's surface tension[32]. BFO has been synthesized by glycine fuel through microwave-assisted solution combustion with some impurity phases such as $Bi_2Fe_4O_9$ and $Bi_{24}Fe_2O_{39}$[33]. In our previous works, BFO was synthesized using various single and mixed fuels at a constant fuel to oxidant ratio of 1, but in this work different fuel-to-oxidant ratios (φ) were varied from 0.5 to 2[32–34].

Nevertheless, combining different fuels might be more effective than individual fuels via improved control over the reaction temperature, the type, and the amount of gaseous products released. Therefore, in this work, glycine and CTAB were mixed at various fuel-to-oxidant amounts in the uni-molar ratio to synthesize nearly pure and single-phase BFO.

School of Metallurgy and Materials Engineering, Iran University of Science and Technology (IUST), Narmak, Tehran, Iran. ✉email: mhashemi@iust.ac.ir

Experimental procedure

Synthesis route. Analytical grades Fe(NO3)3.9H2O, Bi(NO3)2.5H2O, CTAB [(C16H33)N(CH3)3]Br (> 99%), glycine (C2H5NO2), were purchased from Merk Co. without any further purification. Whereby HNO3 (68 wt %) was added to dissolve bismuth nitrate. The required amount of Bi(NO3)0.5H2O and Fe(NO3)0.9H2O, cetyltrimethylammonium bromide ([(C16H33)N(CH3)3]Br), and glycine (C2H5NO2) were prepared by dissolving 15 mL of 3 mol L^{-1} of HNO3 in various fuel-to-oxidant ratios of ($\varphi = 0.5$, 0.75, 1 and 2). H_2O, CO_2, Br_2, and N_2 are assumed to be the gaseous products of the combustion reaction, where the type of gaseous products and adiabatic temperature are controlled by the fuel-to-oxidant ratio (φ).

$$Bi(NO_3)_3 + Fe(NO_3)_3 + \frac{1}{2}\left(\frac{15}{59}\varphi\, C_{19}H_{36}NBr + \frac{10}{3}\varphi\, C_2H_5NO_2\right) + \frac{15}{2}(\varphi - 1)\, O_2 \rightarrow BiFeO_3 + \frac{2035}{354}\varphi CO_2 + \frac{2285}{354}\varphi H_2O + \left(3 + \frac{635}{708}\varphi\right)N_2 + \frac{15}{236}\varphi\, Br_2$$

8500S SHIMADZU spectrophotometer recorded IR spectra in the range of (400–4000 cm^{-1}). Differential thermal (DTA) and thermogravimetry analysis (TGA) were used to study the combustion behavior in the air with a heating rate of 5 °C/min on an STA Ba¨HR 503 instrument. Microstructure and phase evolution were examined by X-ray diffraction (PANalytical X'pert, CuKa = 1.54060 A°). Crystallite sizes were also calculated using the raw data from XRD using the Williamson-Hall method. Field emission scanning electron microscopy (FESEM) was acquired to characterize the morphology of the as-combusted powders by TESCAN Vega II. UV–Vis diffuse reflectance spectrum (DRS) was acquired to measure the bandgap and visible light absorption of the powders by a Shimadzu UV–Vis 52550 spectrophotometer in the wavelength range of (300–800 nm). A Tauc's plot is used to determine the optical bandgap of semiconductors. Typically, a Tauc's plot shows the quantity hν (the photon energy) on the (x-coordinate) and the quantity $(\alpha h\nu)^{1/2}$ on the (y-coordinate), where α is the absorption coefficient of the material. Thus, extrapolating this linear region to the abscissa yields the energy of the optical bandgap of the semiconductor material.

Photocatalytic performance. In the presence of combusted BFO powders, the methylene blue (MB) dye was broken down by visible light irradiation from two 100 W Xenon lamps with a cutoff ultraviolet filter.100 mg of BFO catalyst was dispersed in 100 mL of methylene blue (15 mg/L) in the company of 0.1 mL of H_2O_2 (30%) and stirred for 60 min in the dark to obtain the adsorption/desorption equilibrium. Furthermore, the pH of the solution was adjusted by HCl (37 wt%). BFO powders were separated by centrifugation at 6000 rpm for 10 min, followed by MB concentration monitoring on a PG Instruments Ltd. T80-UV/Vis spectrophotometer.

Results and discussion:

Figure 1 illustrates the thermal analysis of dried gel produced by a mixture of glycine and CTAB fuels at $\varphi = 1$. A slight drop (~ 9%) in the gel's mass is possibly due to the evaporation of absorbed water. A sharp decline at about 178 °C, possibly triggered by the exothermic reaction between metal nitrates and glycine CTAB fuels. This enormous drop (~ 70%) in the gel mass is because of a combustion reaction that released a large amount of gaseous products such as CO_2, H_2O, N_2, Br_2, etc.

Based on previous findings[34–36], glycine has a lower decomposition temperature compared to CTAB, with a fast combustion reaction rate showing sharp weight loss in the gel. Similarly, when the mixture of glycine and CTAB is used as a fuel, colossal weight loss seems to be dominated by the presence of glycine rather than CTAB. Furthermore, a smaller exothermic peak at 285 °C with a gradual weight loss might be attributed to the slow oxidation reaction of residual organics that remained in the gel[37].

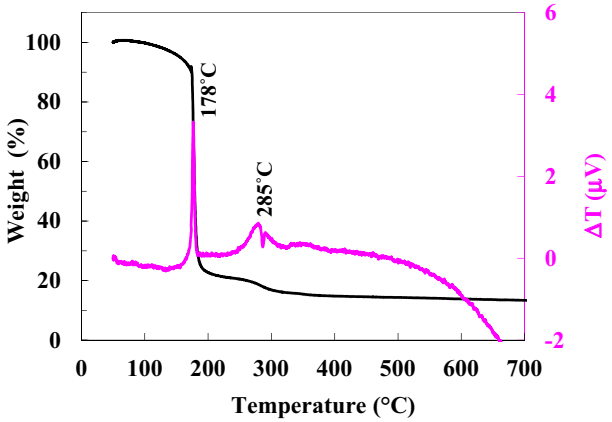

Figure 1. TGA/DTA curves of the dried gel prepared by a mixture of CTAB and glycine fuels at $\varphi = 1$.

The FTIR spectra of dried gel and as-combusted powders prepared by the glycine and CTAB fuel mixture at $\varphi = 1$ are illustrated in Fig. 2. The broad vibrational stretching modes in the range of 3200–3700 cm^{-1} correspond to the absorption of hydroxyl groups of water molecules that are omitted in the combusted BFO powders[38]. The stretching vibration of C-H bonds in CTAB molecules can lead to the formation of bands at 2920 and 2850 cm^{-1}[39]. The vibrational band at 1350 cm^{-1} is due to the attachment of CO_3^{2-} groups to the cations[38]. The adsorption bands at 1650 cm^{-1}, 1360 cm^{-1}, 902 cm^{-1}, 802 cm^{-1}, and 730 cm^{-1} confirm the formation of NO_3^- connected to the CTAB and glycine molecules in the dried gel[40]. Stretching bands at 1757 cm^{-1} and 1556 cm^{-1} resemble the existence of COO^- groups formed through the oxidation of CTAB molecules[41]. Peaks at 1105 cm^{-1} and 1020 cm^{-1} confirm the presence of NH_2 groups. Carboxylate groups can chelate cations, leading to the absorption band at 586 cm^{-1}, which corresponds to metal–oxygen bonds[42]. Strong peaks at 557 cm^{-1} and 465 cm^{-1} of combusted powder can be assigned to the vibrational bending and stretching of Fe–O in the octahedral FeO6 groups in the perovskite structure[43].

XRD patterns of conventionally combusted BFO powders at the various φ values are depicted in Fig. 3. The combusted powders at $\varphi = 0.5$ and $\varphi = 0.75$ are semi-amorphous due to their incomplete combustion reaction and low adiabatic combustion temperature. $Bi_2Fe_4O_9$ (JCDPS Card No. 00-020-0836) impurity phase is presented at φ values of 0.5 and 0.75. However, maximum adiabatic temperature occurs at $\varphi = 1$, leading to a well crystalline pattern. $Bi_{24}Fe_2O_{39}$ (JCDPS Card No. 00-042-0201) was the only impurity phase formed at the φ values of 1 and 2.

Bi_2O_3 and Fe_2O_3, as the transitional phases, can take part in the solid reaction of ($Bi_2O_3 + Fe_2O_3 \rightarrow 2\ BiFeO_3$) to produce the $BiFeO_3$ phase. Nevertheless, the formation of impurity phases such as $Bi_2Fe_4O_9$ and $Bi_{24}Fe_2O_{39}$ can be ascribed to the insufficiency of Bi_2O_3 and Fe_2O_3 phases initiated by the phase segregation[44]:

$$Bi_2O_3 + 2\ Fe_2O_3 \rightarrow Bi_2Fe_4O_9$$

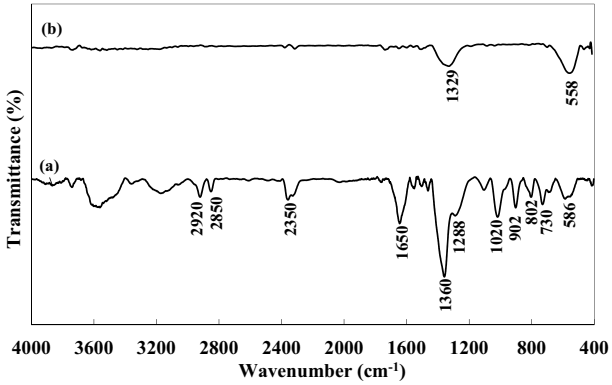

Figure 2. FTIR spectra of (**a**) dried gel and (**b**) the as-combusted BFO powders at $\varphi = 1$.

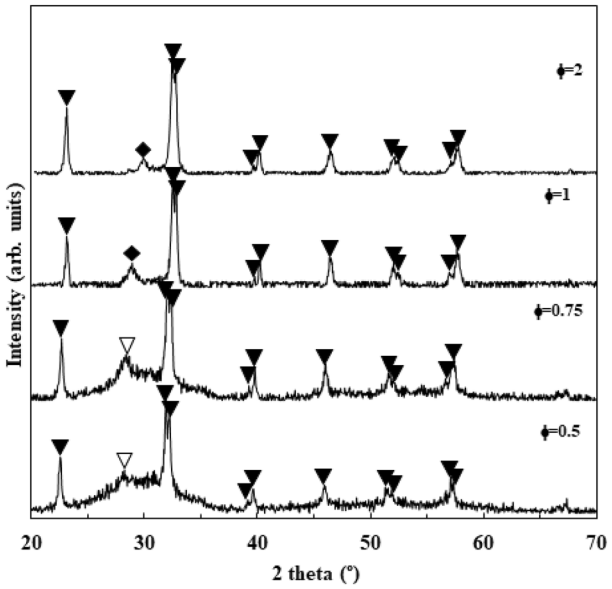

Figure 3. XRD patterns of the as-combusted BFO powders using glycine and CTAB fuel content. (filled down pointing triangle: $BiFeO_3$, open down pointing triangle: $Bi_2Fe_4O_9$, filled diamond: $Bi_{24}Fe_2O_{39}$).

$$12\ Bi_2O_3 + Fe_2O_3 \rightarrow Bi_{24}Fe_2O_{39}$$

The inferior crystallinity of as-combusted powders due to their lower combustion temperatures can be improved by further calcination at higher temperatures (Fig. 4). Impurity phases were mainly eliminated by one-hour calcination at 600 °C due to the reaction of the residual Bi_2O_3 and Fe_2O_3 phases.

$$Bi_2O_3 + Bi_2Fe_4O_9 \rightarrow 4\ BiFeO_3$$

$$11\ Fe_2O_3 + Bi_{24}Fe_2O_{39} \rightarrow 24BiFeO_3$$

SEM micrographs of BFO powders synthesized at different φ values are illustrated in Fig. 5. As combusted powders display a bulky microstructure, the particle sizes are reduced from 37 to 18 nm with the increase in fuel content presented in Table 1, as calculated from XRD data using the Williamson-Hall technique. Particle size mainly depends on the combustion temperature and reaction rate, where the combustion rate would influence the number of nucleation sites and higher combustion temperature enhances the particle growth[45]. When the fuel content is increased, a higher amount of generated heat is consumed by the combustion gases and hence reduces the adiabatic temperature. This decline in the adiabatic temperature resulted in particle size refinement. However, as seen in Fig. 5d–f, calcined powders exhibit particle size growth as a result of the rise in the temperature.

Another proposed reason behind this particle size refinement at higher CTAB/glycine content, as illustrated schematically in Fig. 6, could be due to the interaction of CTAB micelles with the cationic head inside the solution precursor, separated a large amount of the cationic ends apart and produced smaller BFO nanoparticles when the CTAB amount was maximized. Figure 7a displays diffuse reflectance spectra of the as combusted BFO powders. The amount of visible light absorption mainly depends on the crystallinity, strain, particle size, impurity phases, etc. The crystal field and metal–metal transitions affect the absorption spectra[46]. The increase in light absorption at higher fuel content (φ = 2) is possibly due to the decrease in the impurity phase $Bi_{24}Fe_2O_{39}$. However, powders synthesized at fuel content of (φ = 0.75) significantly absorbed a higher amount of visible light, probably due to the formation of distinct impurity phase of $Bi_2Fe_4O_9$, as previously discussed in XRD data. The Tauc's plot measured bandgap energy of the combusted powders $((\alpha h\upsilon)^2$ vs. hυ), as shown in Fig. 7b and summarized in Table 1. The bandgap energies of the combusted BFO powders are in the range of 1.85–1.96 eV, in good agreement with the bandgap of powders and thin films reported in the literature[46]. At higher fuel contents, the decrease in bandgap energy is mainly due to the particle size refinement, while the increase in the bandgap energy at φ = 2 could be owed to the presence of the impurity phase $Bi_{24}Fe_2O_{39}$.

The relative concentrations (C/C_0) of MB, as an organic pollutant, versus visible light irradiation is illustrated in Fig. 8. The MB is photodegraded by about 80% during 90 min of visible light illumination for combusted powders at φ values of 2 and 0.75. However, the degradation rate is slightly higher for the combusted powders synthesized at φ = 2. Based on our previous findings[32,33], the combusted powders synthesized by pure glycine or pure CTAB only showed the photodegradation of MB at about 50 and 30 percent, respectively. Therefore, by mixing the glycine and CTAB fuels, the photodegradation of MB is profoundly enhanced possibly due to the particle size refinement and higher crystallinity with less amount of impurity phases being present. The oxidation of MB dye molecule to CO_2 and H_2O species mainly depends on the presence of active species such as O^{-2}, OH radicals[47]. The photogenerated electrons and holes during the light absorption of powders would react with the

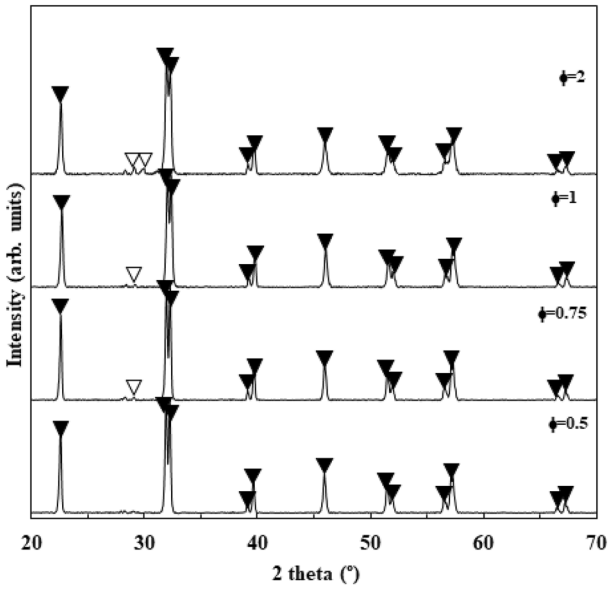

Figure 4. XRD patterns of the as-calcined BFO powders using glycine and CTAB fuel content (filled down pointing triangle: $BiFeO_3$, open down pointing triangle: $Bi_2Fe_4O_9$).

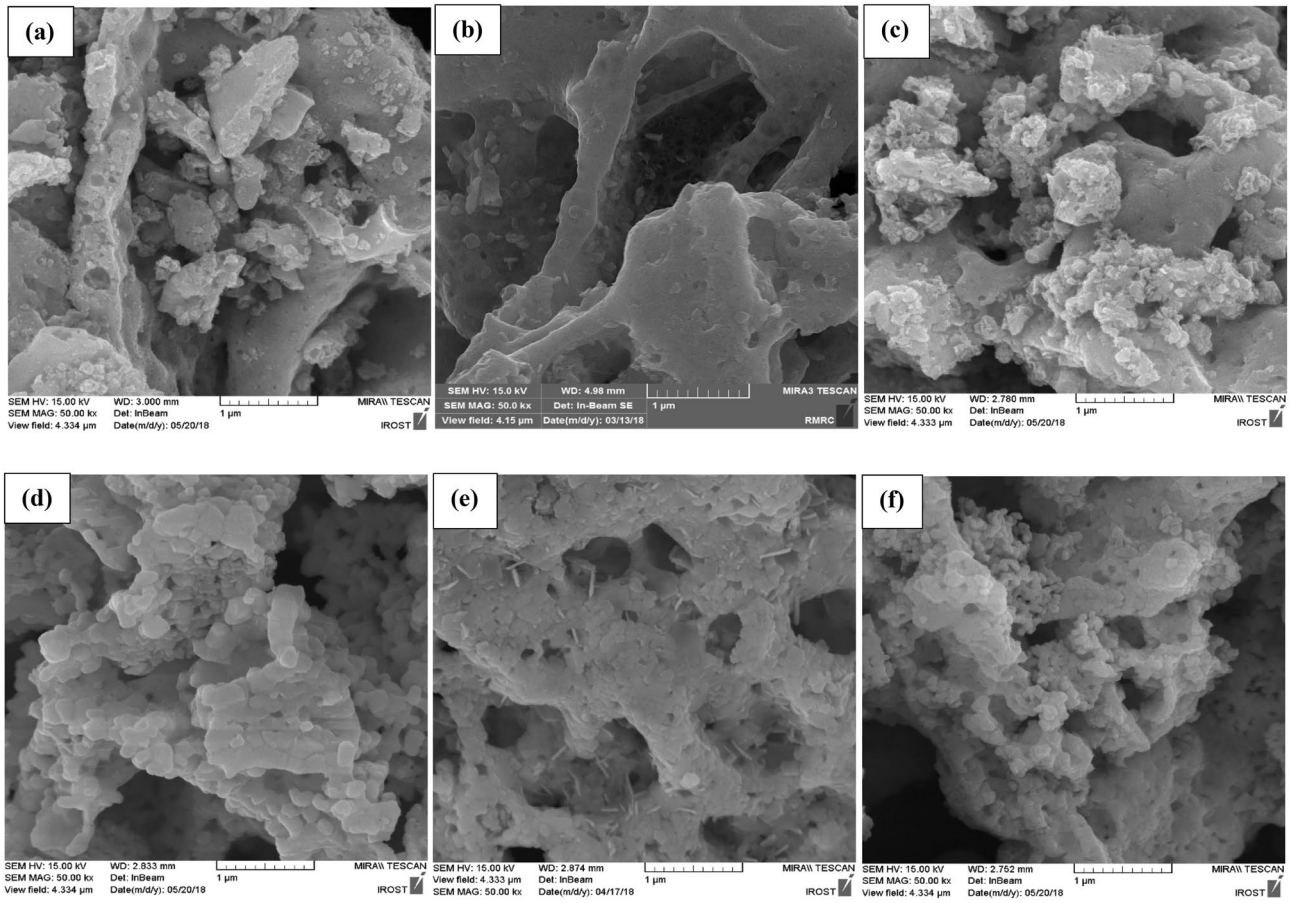

Figure 5. SEM micrographs of the as-combusted BFO powders at (**a**) φ = 0.75, (**b**) φ = 1 and (**c**) φ = 2 and the as-calcined BFO powders at (**d**) φ =0.75, (**e**) φ =1 and (**f**) φ =2.

As-combusted	D_{XRD} (nm)	Eg (eV)
0.5	37	1.96
0.75	28	1.85
1	21	1.96
2	18	1.96

Table 1. Crystallite size (D_{XRD}) of $BiFeO_3$ phase, and bandgap energy (Eg) as a function of fuel type.

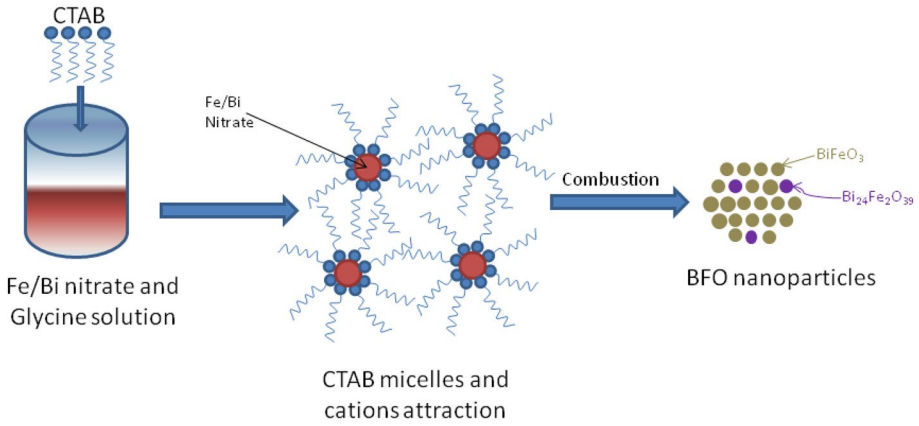

Figure 6. Schematic of BFO nanoparticle synthesis via micells formation at high CTAB content.

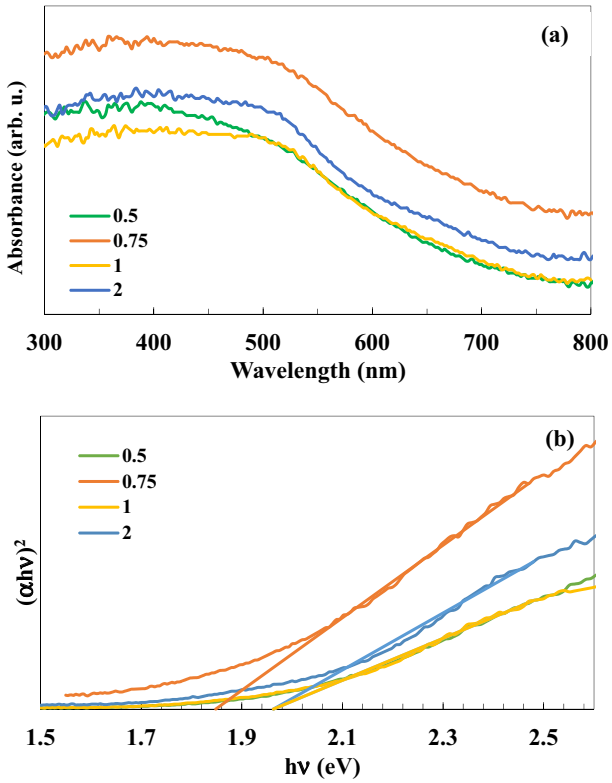

Figure 7. (**a**) UV–Vis diffuse reflectance spectra and (**b**) Tauc's plot of the as-combusted BFO powders.

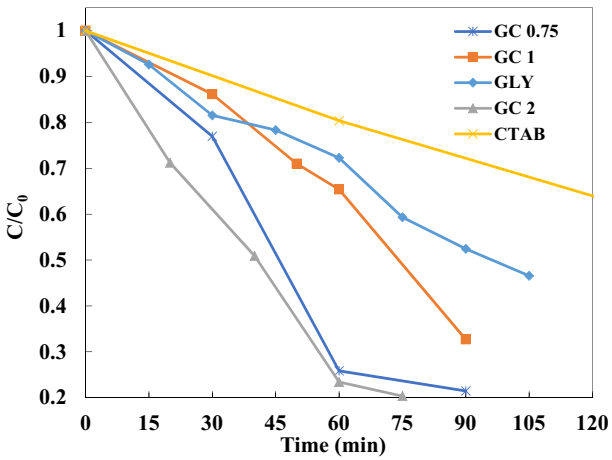

Figure 8. C/C_0 versus irradiation time in the presence of the BFO powders at different fuel content and type.

oxygen and water molecules to produce the active species. Thus, the optical properties of combusted powders such as bandgap energy, absorption coefficient, and band edge position play an important role in photocatalytic performance[48].

Conclusions

High purity BFO powders were synthesized via solution combustion synthesis by the mixture of glycine and CTAB as fuels at different fuel contents. The amount of the impurity phase was reduced by increasing fuel content from 0.5 to 2. $Bi_2Fe_4O_9$ impurity phase was present at φ values of 0.5 and 0.75. However, at higher fuel ratios (φ values of 1 and 2), the impurity phase was transformed into the $Bi_{24}Fe_2O_{39}$ phase.

The combusted powders at φ values of 2 and 0.75 showed the highest MB photodegradation of about 80% under 90 min of visible light illumination mainly due to the particle size refinement, higher visible light

absorption, and less amount of impurities. Furthermore, the photodegradation rate of combusted powders synthesized at $\varphi = 2$ was somewhat enhanced.

Data availability

The datasets used and/or analysed during the current study available from the corresponding author on reasonable request.

Received: 15 June 2023; Accepted: 27 July 2023
Published online: 31 July 2023

References

1. Shokrollahi, H. Magnetic, electrical and structural characterization of $BiFeO_3$ nanoparticles synthesized by co-precipitation. *Powder Technol.* **235**, 953–958 (2013).
2. Vanga, P. R., Mangalaraja, R. V. & Ashok, M. Structural, magnetic and photocatalytic properties of La and alkaline co-doped $BiFeO_3$ nanoparticles. *Mater. Sci. Semicond. Process.* **40**, 796–802 (2015).
3. Chen, S. *et al.* Hand-fabricated CNt/AgNps electrodes using Wax-on-plastic platforms for electro-immunosensing application. *Sci. Rep.* **9**(1), 6131 (2019).
4. Xu, X., Wang, W., Zhou, W. & Shao, Z. Recent advances in novel nanostructuring fthrumethods of perovskite electrocatalysts for energy-related applications. *Small Methods* **2**, 1800071 (2018).
5. He, J., Xiaomin, Xu., Li, M., Zhou, S. & Zhou, W. Recent advances in perovskite oxides for non-enzymatic electrochemical sensors: A review. *Anal. Chim. Acta* **1251**, 341007 (2023).
6. Yang, L. *et al. ACS Sustain. Chem. Eng.* **10**(5), 1899–1909 (2022).
7. Guo, R., Fang, L., Dong, W., Zheng, F. & Shen, M. Enhanced photocatalytic activity and ferromagnetism in Gd doped $BiFeO_3$ nanoparticles. *J. Phys. Chem. C* **114**(49), 21390–21396 (2010).
8. Chen, Y., Tang, Y., Luo, S., Liu, C. & Li, Y. TiO2 nanotube arrays co-loaded with Au nanoparticles and reduced graphene oxide: facile synthesis and promising photocatalytic application. *J. Alloys Compd.* **578**, 242–248 (2013).
9. Zhang, Y. *et al.* Combination of photoelectrocatalysis and adsorption for removal of bisphenol A over TiO_2-graphene hydrogel with 3D network structure. *Appl. Catal. B Environ.* **221**, 36–46 (2018).
10. Nag, A., Sapra, S., Chakraborty, S., Basu, S. & Sarma, D. D. Synthesis of CdSe nanocrystals in a noncoordinating solvent: effect of reaction temperature on size and optical properties. *J. Nanosci. Nanotechnol.* **7**(6), 1965–1968 (2007).
11. Rajeshwar, K. *et al.* Heterogeneous photocatalytic treatment of organic dyes in air and aqueous media. *J. Photochem. Photobiol. C Photochem. Rev.* **9**(4), 171–192 (2008).
12. Herrmann, J.-M. Heterogeneous photocatalysis: fundamentals and applications to the removal of various types of aqueous pollutants. *Catal. Today* **53**(1), 115–129 (1999).
13. Fu, Y. & Wang, X. Magnetically separable $ZnFe_2O_4$–graphene catalyst and its high photocatalytic performance under visible light irradiation. *Ind. Eng. Chem. Res.* **50**(12), 7210–7218 (2011).
14. Vahdat Vasei, H., Masoudpanah, S. M., Adeli, M. & Aboutalebi, M. R. Photocatalytic properties of solution combustion synthesized ZnO powders using mixture of CTAB and glycine and citric acid fuels. *Adv. Powder Technol.* **30**(2), 284–291 (2019).
15. Singh, H., Garg, N., Arora, P. & Rajput, J. K. Sucrose chelated auto combustion synthesis of $BiFeO_3$ nanoparticles: Magnetically recoverable catalyst for the one-pot synthesis of polyhydroquinoline. *Appl. Organometal Chem.* **32**, e4357 (2018).
16. Kumar, S. S., Rao, K., Krishnaveni, T., Goud, A. & Reddy, P. Solution Combustion Synthesis and Characterization of Nanosized Bismuth Ferrite. *AIP Conf. Proc.* **1447**, 339–340 (2011).
17. Ilić, N. *et al.* Auto-combustion synthesis as a method for preparing $BiFeO_3$ powders and flexible $BiFeO_3$/PVDF films with improved magnetic properties Influence of doping ion position, size and valence on electric properties. *Mater. Sci. Eng.: B* **280**, 115686 (2022).
18. Paborji, F., Shafiee Afarani, M., Arabi, A. M. & Ghahari, M. Solution combustion synthesis of $FeCr_2O_4$ powders for pigment applications: Effect of fuel type. *Int. J. Appl. Ceram. Technol.* **19**, 2406–2418 (2022).
19. Paborji, F., Shafiee Afarani, M., Arabi, A. M. & Ghahari, M. Solution combustion synthesis of $FeCr_2O_4$:Zn, Al pigment powders. *Int. J. Appl. Ceram. Technol.* **20**, 2203–2216 (2023).
20. Gao, T. *et al.* Shape-controlled preparation of bismuth ferrite by hydrothermal method and their visible-light degradation properties. *J. Alloys Compd.* **648**, 564–570 (2015).
21. Wang, X. *et al.* PVP assisted hydrothermal fabrication and morphology-controllable fabrication of $BiFeO_3$ uniform nanostructures with enhanced photocatalytic activities. *J. Alloys Compd.* **677**, 288–293 (2016).
22. Wang, Y. *et al.* Low temperature polymer assisted hydrothermal synthesis of bismuth ferrite nanoparticles. *Ceram. Int.* **34**(6), 1569–1571 (2008).
23. Gao, T. *et al.* Synthesis of $BiFeO_3$ nanoparticles for the visible-light induced photocatalytic property. *Mater. Res. Bull.* **59**, 6–12 (2014).
24. Ke, H. *et al.* Factors controlling pure-phase multiferroic $BiFeO_3$ powders synthesized by chemical co-precipitation. *J. Alloys Compd.* **509**(5), 2192–2197 (2011).
25. Bo, H. Y., Tan, G. Q., Miao, H. Y. & Xia, A. Co-precipitation synthesis of $BiFeO_3$ powders. *Adv. Mater. Res.* **105**, 286–288 (2010).
26. Liu, Z., Qi, Y. & Lu, C. High efficient ultraviolet photocatalytic activity of $BiFeO_3$ nanoparticles synthesized by a chemical coprecipitation process. *J. Mater. Sci. Mater. Electron.* **21**(4), 380–384 (2010).
27. Wang, W. *et al.* Electrospinning of magnetical bismuth ferrite nanofibers with photocatalytic activity. *Ceram. Int.* **39**(4), 3511–3518 (2013).
28. Huo, Y., Jin, Y. & Zhang, Y. Citric acid assisted solvothermal synthesis of $BiFeO_3$ microspheres with high visible-light photocatalytic activity. *J. Mol. Catal. A Chem.* **331**(1–2), 15–20 (2010).
29. Yang, J. *et al.* Factors controlling pure-phase magnetic $BiFeO_3$ powders synthesized by solution combustion synthesis. *J. Alloys Compd.* **509**(37), 9271–9277 (2011).
30. Aruna, S. T. & Mukasyan, A. S. Combustion synthesis and nanomaterials. *Curr. Opin. Solid State Mater. Sci.* **12**(3–4), 44–50 (2008).
31. Motevalian, A. & Salem, S. Effect of glycine–starch mixing ratio on the structural characteristics of $MgAl_2O_4$ nano-particles synthesized by sol–gel combustion. *Particuology* **24**, 108–112 (2016).
32. Asefi, N., Hasheminiasari, M. & Masoudpanah, S. M. Solution combustion synthesis of $BiFeO_3$ powders using CTAB as fuel. *J. Electron. Mater.* **48**, 1–7 (2018).
33. Asefi, N., Masoudpanah, S. M. & Hasheminiasari, M. Microwave-assisted solution combustion synthesis of $BiFeO_3$ powders. *J. Sol-Gel Sci. Technol.* **86**, 1–9 (2018).
34. Asefi, N., Masoudpanah, S. M. & Hasheminiasari, M. Photocatalytic performances of $BiFeO_3$ powders synthesized by solution combustion method: The role of mixed fuels. *Mater. Chem. Phys.* **228**, 168–174 (2019).
35. Huang, J. *et al.* Microwave hydrothermal synthesis of $BiFeO_3$: Impact of different surfactants on the morphology and photocatalytic properties. *Mater. Sci. Semicond. Process.* **25**, 84–88 (2014).

36. Joshi, U. A., Jang, J. S., Borse, P. H. & Lee, J. S. Microwave synthesis of single-crystalline perovskite $BiFeO_3$ nanocubes for photoelectrode and photocatalytic applications. *Appl. Phys. Lett.* **92**(24), 242106 (2008).
37. Radpour, M., Masoudpanah, S. M. & Alamolhoda, S. Microwave-assisted solution combustion synthesis of Fe_3O_4 powders. *Ceram. Int.* **43**(17), 14756–14762 (2017).
38. Socrates, G. *Infrared and Raman Characteristic Group Frequencies, 3rd edn.,* (Wiley, 2001).
39. Hamedani, S. F. N., Masoudpanah, S. M., Bafghi, M. S. & Baloochi, N. A. Solution combustion synthesis of $CoFe_2O_4$ powders using mixture of CTAB and glycine fuels. *J. Sol-Gel Sci. Technol.* **86**(3), 743–750 (2018).
40. Naderi, P., Masoudpanah, S. M. & Alamolhoda, S. Magnetic properties of $Li_{0.5}Fe_{2.5}O_4$ nanoparticles synthesized by solution combustion method. *Appl. Phys. A* **123**(11), 702 (2017).
41. Shabani, S., Mirkazemi, S. M., Masoudpanah, S. M. & Abadi, P. T. D. Synthesis and characterization of pure single phase $BiFeO_3$ nanoparticles by the glyoxylate precursor method. *J. Supercond. Nov. Magn.* **27**(12), 2795–2801 (2014).
42. Ortiz-Quiñonez, J. L. *et al.* Easy synthesis of high-purity $BiFeO_3$ nanoparticles: New insights derived from the structural, optical, and magnetic characterization. *Inorg. Chem.* **52**(18), 10306–10317 (2013).
43. Masoudpanah, S. M., Mirkazemi, S. M., Bagheriyeh, R., Jabbari, F. & Bayat, F. Structural, magnetic and photocatalytic characterization of $Bi_{1-x}La_xFeO_3$ nanoparticles synthesized by thermal decomposition method. *Bull. Mater. Sci.* **40**(1), 93–100 (2017).
44. Feng, K., Wang, L.-C., Lu, J., Wu, Y. & Shen, B.-G. Experimentally determining the intrinsic center point of Bi_2O_3–Fe_2O_3 phase diagram for growing pure $BiFeO_3$ crystals. *CrystEngComm* **15**(24), 4900–4904 (2013).
45. Deganello, F. & Tyagi, A. K. Solution combustion synthesis, energy and environment: Best parameters for better materials. *Prog. Cryst. Growth Charact. Mater.* **64**(2), 23–61 (2018).
46. Lam, S.-M., Sin, J.-C. & Mohamed, A. R. A newly emerging visible light-responsive $BiFeO_3$ perovskite for photocatalytic applications: A mini review. *Mater. Res. Bull.* **90**, 15–30 (2017).
47. Prashanthi, K., Thakur, G. & Thundat, T. Surface enhanced strong visible photoluminescence from one-dimensional multiferroic $BiFeO_3$ nanostructures. *Surf. Sci.* **606**(19–20), L83–L86 (2012).
48. Soltani, T. & Entezari, M. H. Photolysis and photocatalysis of methylene blue by ferrite bismuth nanoparticles under sunlight irradiation. *J. Mol. Catal. A Chem.* **377**, 197–203 (2013).

Author contributions

N.A. performed the experimental part and wrote the draft of the paper. M.H. supervised the research and wrote and edited the paper. S.M.M. supervised the research and wrote and edited the paper.

Competing interests

The authors declare no competing interests.

Additional information

Correspondence and requests for materials should be addressed to M.H.

Reprints and permissions information is available at www.nature.com/reprints.

Publisher's note Springer Nature remains neutral with regard to jurisdictional claims in published maps and institutional affiliations.